American Journal of Advanced Materials Research (AJAMR)

ISSN: 3070-2011 (ONLINE)

VOLUME 2 ISSUE 1 (2026)

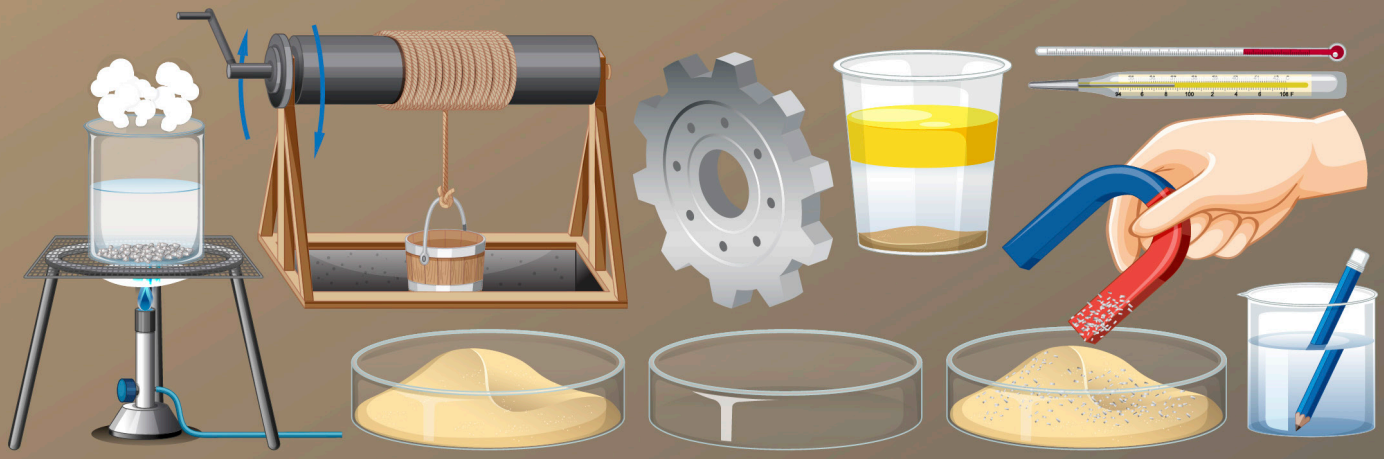

PUBLISHED BY
E-PALLI PUBLISHERS, DELAWARE, USA

American Journal of
Advanced Materials Research (AJAMR)

Volume 2 Issue 1, Year 2026
ISSN: 2158-8155 (Online), 2832-4854 (Print)
DOI: https://doi.org/10.54536/ajamr.v2i1.7398
https://journals.e-palli.com/home/index.php/ajamr

Proton Therapy: Analytical Formulation of Three-Dimensional Geometric Tumor Regression in Pediatric Medulloblastoma by Magnetic Resonance Imaging

Matheus dos Santos Farias[1*]

Article Information

Received: February 27, 2026

Accepted: April 04, 2026

Published: June 04, 2026

Keywords

Differential Equations,
Magnetic Resonance Imaging,
Mathematical Modeling,
Pediatric Medulloblastoma,
Proton Therapy

ABSTRACT

Despite the major importance of medical imaging in pediatric neuro-oncology, there is still a limited connection between clinical image interpretation and rigorous mathematical formalism. Pediatric medulloblastoma is usually described through radiological, surgical, and pathological findings, while its geometric evolution is rarely translated into a quantitative and reproducible framework. This study addresses that gap by proposing an innovative mathematical approach based on real clinical imaging data from the literature. Starting from classical tumor-growth theory, the work develops a regression-oriented model based on differential equations to describe the three-dimensional evolution of the lesion. The tumor is approximated by simplified analytical geometries, allowing its dimensions to be incorporated into a tractable volumetric framework. Numerical implementation in Python was then used to generate three-dimensional representations consistent with the radiological states reported in the clinical case. The results show that qualitative imaging findings can be converted into measurable mathematical objects, improving the interpretation of tumor burden and residual disease. The study also demonstrates that mathematical language can move beyond abstraction and become a practical tool for quantitative medical imaging. In this sense, the work contributes to an underexplored field by linking medical physics, applied mathematics, and pediatric oncology through a clinically meaningful modeling strategy.

INTRODUCTION

Cancer in the World

Worldwide, an estimated 20 million new cancer cases were diagnosed in 2022. The most frequently diagnosed cancer types were lung cancer (12.4%), female breast cancer (11.6%), colorectal cancer (9.6%), prostate cancer (7.3%), and stomach cancer (4.9%) (Bray *et al.,* 2024).

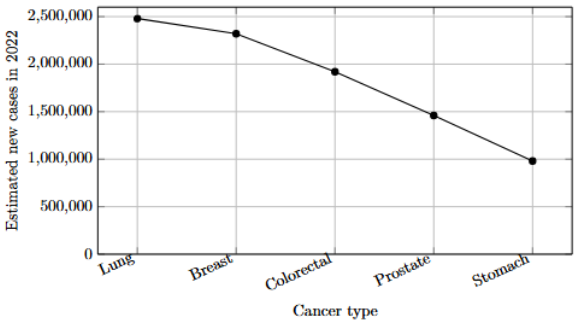

Figure 1: Estimated global incidence of the main cancer types in 2022

Cancer in Brazil

Brazil is expected to register approximately 704,000 new cancer cases per year during the 2023–2025 triennium. Excluding non-melanoma skin cancer, the most incident tumor types are female breast cancer (73,610 cases), prostate cancer (71,730 cases), colorectal cancer (45,630 cases), lung cancer (32,560 cases), and stomach cancer (21,480 cases) (Santos *et al.,* 2023).

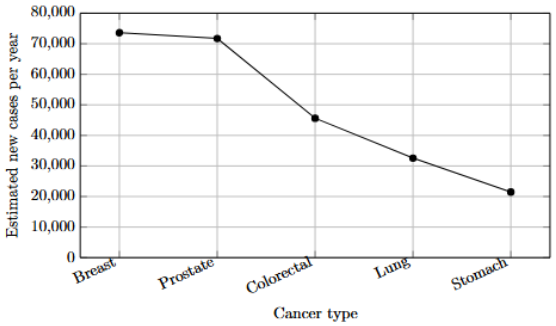

Figure 2: Estimated annual incidence of the main cancer types in Brazil for the 2023–2025 triennium

Central Nervous System Tumors in Childhood

Central nervous system tumors are among the most relevant solid neoplasms in pediatric oncology, and Brazilian population-based registries reported a median incidence of 20.49 cases per million children aged 0–14 years for pediatric CNS tumors. Although medulloblastoma is not among the most frequent cancers in the general population, it deserves special attention because it is one of the most important malignant brain tumors in childhood (Oigman *et al.,* 2022).

Medulloblastoma is the most common malignant pediatric CNS tumor and remains clinically challenging because of its marked biological heterogeneity, variable prognosis, risk of neuraxial dissemination, and substantial long-term treatment-related morbidity among survivors.

[1] Medical Physics, Hospital Albert Einstein, São Paulo, Brazil
[*] Corresponding author's e-mail: matheusfariasfm@gmail.com

For this reason, it represents a highly relevant model for quantitative and imaging-based analysis in pediatric neuro-oncology (Cooney *et al.,* 2022).

Pediatric Medulloblastoma: Clinical Relevance

Pediatric medulloblastoma is the most common malignant brain tumor of childhood and remains clinically significant because it comprises biologically distinct subgroups with different prognoses, patterns of dissemination, and therapeutic responses (Cooney *et al.,* 2023).

Its clinical relevance is further reinforced by the persistent burden of treatment-related toxicity, including neurocognitive, endocrine, and quality-of-life impairments among long-term survivors, which justifies continued investigation into safer and more precise therapeutic strategies (Cooney *et al.,* 2023).

From a research perspective, medulloblastoma has attracted increasing scientific attention; a bibliometric analysis identified 4,058 articles published up to 2020 and demonstrated a marked rise in annual output, particularly during the last decade (Alcantara *et al.,* 2023).

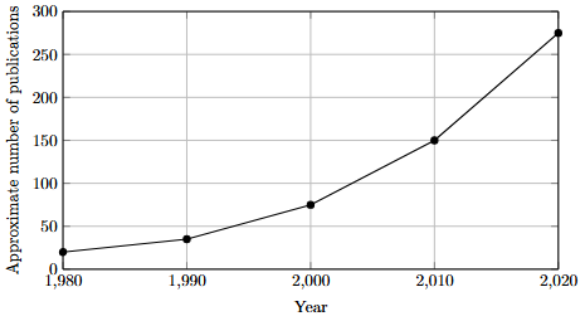

Figure 3: Approximate growth in medulloblastoma-related publications over time, adapted from the bibliometric trend reported by Alcantara *et al.* (2023)

Objective

General Objective

To develop and apply a mathematical model capable of describing the three-dimensional geometric regression of pediatric medulloblastoma based on real magnetic resonance imaging data obtained from published clinical cases involving proton therapy.

Specific Objectives

- To identify and select a published clinical case containing sequential magnetic resonance images of a pediatric patient diagnosed with medulloblastoma.
- To extract geometric information from the reported images in order to represent tumor evolution over time.
- To formulate a mathematical model capable of describing the temporal regression of the lesion based on clinically observed image data.
- To implement the proposed model numerically in Python using simple numerical methods.
- To generate simulated tumor images based on the mathematical model and compare them qualitatively with the magnetic resonance images reported in the clinical case.
- To demonstrate that mathematical language can provide a consistent and relevant framework for the interpretation of real clinical imaging data, thereby helping to fill a gap in the literature regarding the quantitative description of tumor behavior in pediatric neuro-oncology.

Justification

The justification for this study is based on the need to strengthen the dialogue between medical physics, applied mathematics, and pediatric oncology, particularly in the interpretation of magnetic resonance imaging findings in real clinical contexts. Although imaging follow-up plays a central role in the evaluation of tumor response, most clinical descriptions in the literature remain predominantly qualitative, with limited incorporation of mathematical language capable of formally representing the geometric and temporal evolution of the lesion.

In the specific case of pediatric medulloblastoma, this limitation becomes even more relevant because it is a highly important malignant brain tumor in childhood, requiring careful imaging monitoring throughout treatment and follow-up. At the same time, the literature remains relatively scarce with respect to mathematical approaches capable of translating sequential magnetic resonance images into interpretable analytical models based on real clinical data.

Therefore, this study is justified by the proposal to fill part of this gap through the construction of a mathematical framework applied to a published clinical case, using real imaging data as the basis for formal modeling. By combining clinical observation, geometric simplification, differential modeling, and numerical simulation in Python, the present work seeks to demonstrate that mathematical formalism can serve as a complementary tool for understanding tumor regression, thereby contributing to the quantitative interpretation of oncological imaging in the context of pediatric proton therapy.

LITERATURE REVIEW

Fundamentals of Nuclear Physics and Structure of Matter

The structure of matter is organized hierarchically across different physical scales, ranging from the atom to the nucleus and, at a deeper level, to the elementary constituents of hadronic matter. At the atomic scale, matter is characterized by dimensions on the order of 10^{-8} cm, whereas the nucleus occupies a much smaller region, typically around 10^{-12} cm. Protons and neutrons, which compose the nucleus, are themselves structured particles with characteristic dimensions near 10^{-13} cm, while quarks correspond to an even more fundamental level of description (Particle Data Group, 2019).

The electron was identified by J. J. Thomson in 1897 through cathode-ray experiments, providing the first evidence that the atom contained smaller charged constituents (Nobel Prize Outreach, n.d.-b).

The atomic nucleus was established by Ernest Rutherford in 1911 after the gold-foil experiment, which demonstrated that most of the atomic mass is concentrated in a very small central region (Encyclopaedia Britannica, n.d.-b).

The proton was recognized from Rutherford's transmutation experiments in 1917 and became understood as the fundamental positively charged constituent of the nucleus (Encyclopaedia Britannica, n.d.-a).

The neutron was discovered by James Chadwick in 1932, completing the basic nuclear model and explaining the neutral contribution to atomic mass and nuclear stability (Nobel Prize Outreach, n.d.-a).

At a deeper subnuclear level, quarks were independently proposed by Murray Gell-Mann and George Zweig in 1964 as the elementary constituents of hadrons, including protons and neutrons (CERN, 2014).

Figure 4 illustrates this hierarchical organization of matter and highlights the progressive reduction in scale from the atom to quarks.

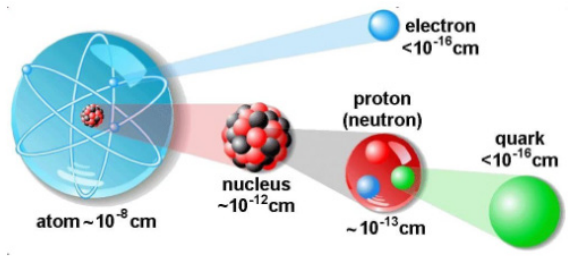

Figure 4: Schematic representation of the structure of matter across different physical scales, from the atom to quarks

Physical Properties of Charged Particles

Charged particles interact with matter primarily through Coulomb forces, losing energy continuously along their path by ionization and excitation of atoms and molecules. Their main physical properties of interest in medical physics are charge, mass, kinetic energy, stopping power, and penetration range, since these quantities determine how energy is deposited inside biological tissue (Particle Data Group, 2019).

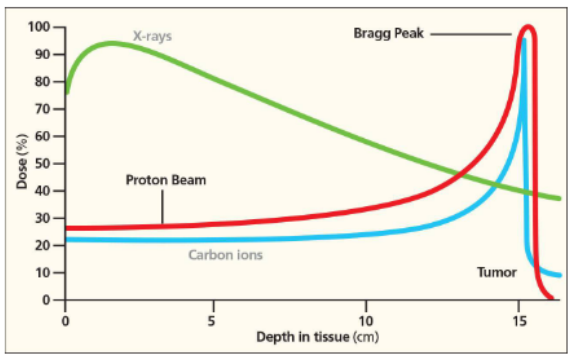

Figure 5: Representative depth–dose profile of charged particles in tissue, illustrating the Bragg peak behavior relevant to proton therapy

In contrast to photons, heavy charged particles such as protons exhibit a finite range in matter and a nonuniform depth–dose distribution, with progressive energy loss followed by a sharp maximum near the end of the track. This characteristic behavior gives rise to the Bragg peak, which is one of the main physical foundations of proton therapy (Massachusetts General Brigham, n.d.).

Figure 5 illustrates the typical depth–dose profile of charged particles in tissue. The curve highlights the increase in deposited dose at greater depths and the steep distal fall-off beyond the peak, a feature that allows better conformity of dose delivery to the tumor volume while reducing irradiation of surrounding healthy tissues (Kraft, 2009).

Interaction of Radiation with Matter

The interaction of radiation with matter is one of the central topics in medical physics because it determines how energy is transferred from radiation to biological tissues. In the case of photon radiation, the main interaction mechanisms are the photoelectric effect, Compton scattering, and pair production, whose predominance depends mainly on photon energy and on the atomic number of the irradiated medium (International Atomic Energy Agency, n.d.).

At lower photon energies, the photoelectric effect is more relevant and contributes strongly to image contrast, especially in high-atomic-number materials. At intermediate energies, Compton scattering becomes dominant and is particularly important in soft tissues, where it reduces image quality by producing scattered radiation. At higher energies, pair production becomes possible when the photon energy exceeds 1.022 MeV (Radiology Key, n.d.).

Figure 6 presents a schematic example of these three main photon interaction processes with matter: photoelectric absorption, Compton scattering, and pair production. This representation is useful because it visually summarizes how the incident photon transfers energy to electrons and, at sufficiently high energies, can generate an electron–positron pair (Radiology Key, n.d.).

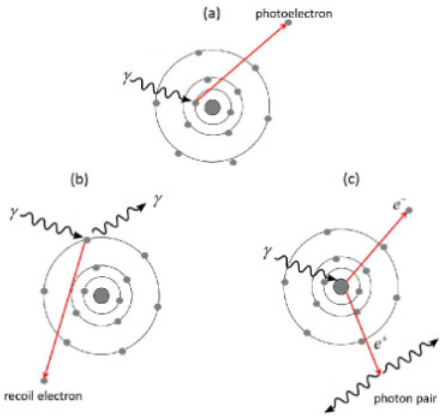

Figure 6: Illustrative scheme of the main photon interaction mechanisms with matter: photoelectric effect, Compton scattering, and pair production

Protons and Fundamentals of Proton Therapy

Protons are positively charged heavy particles whose interaction with matter is characterized by a finite penetration range and by a progressive increase in energy deposition as their velocity decreases. This behavior is described by the stopping power formalism and constitutes the main physical basis for proton therapy (Particle Data Group, 2019).

The therapeutic use of fast protons was proposed by Robert R. Wilson in 1946, who recognized that the controllable range of proton beams could allow highly localized irradiation of deep-seated tumors (Wilson, 1946). In proton therapy, the delivered dose is low at the entrance region, rises gradually with depth, and reaches a maximum close to the end of the particle range, forming the Bragg peak. Beyond this point, the dose falls sharply, with practically no exit dose, which makes proton beams especially attractive for the treatment of tumors located near radiosensitive normal tissues (Massachusetts General Brigham, n.d.).

Figure 7 illustrates a schematic depth–dose comparison between proton therapy and conventional radiation, highlighting the localization of the high-dose region within the tumor volume and the rapid distal fall-off after the Bragg peak.

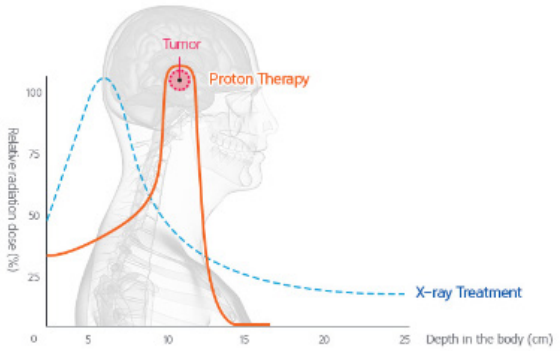

Figure 7: Schematic representation of the depth–dose profile in proton therapy, emphasizing the Bragg peak and its localization within the tumor region

Clinical Applications of Proton Therapy in Pediatrics

Proton therapy has become particularly relevant in pediatric oncology because its physical dose distribution allows high conformity to the target while reducing unnecessary irradiation of surrounding healthy tissues. This characteristic is especially important in children, whose organs and nervous system are still developing and are therefore more vulnerable to long-term radiation-related toxicity (Merchant, 2018).

In clinical practice, proton therapy is commonly considered for pediatric tumors located near critical organs, including brain tumors, skull base lesions, spinal tumors, and cases requiring craniospinal irradiation. Its use is motivated not only by tumor control objectives but also by the need to minimize late effects such as neurocognitive impairment, endocrine dysfunction, growth abnormalities, and secondary malignancies (St. Jude Children's Research Hospital, n.d.).

Figure 8 presents an illustrative example of proton therapy in a pediatric setting. The image highlights the clinical environment in which highly precise beam delivery is performed, emphasizing the practical application of proton therapy as a treatment strategy designed to improve normal tissue sparing in children.

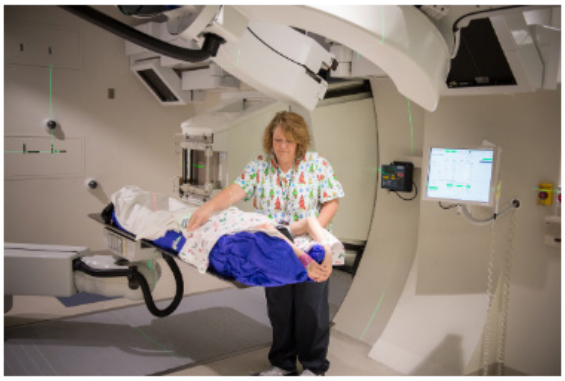

Figure 8: Illustrative example of proton therapy in pediatric oncology

Magnetic Resonance Imaging in Tumor Follow-Up

Magnetic resonance imaging is one of the main tools used in oncological follow-up because it provides high soft-tissue contrast and allows detailed evaluation of lesion morphology, surrounding structures, and treatment-related changes. In neuro-oncology, MRI is particularly important for diagnosis, treatment planning, and post-therapy monitoring of brain tumors (Palumbo *et al.,* 2023; National Cancer Institute, n.d.-b).

In longitudinal follow-up, MRI makes it possible to compare sequential examinations and identify changes in tumor size, geometry, contrast enhancement, edema, and possible signs of recurrence or treatment response. For this reason, it is especially useful in studies that aim to interpret tumor evolution over time using quantitative or mathematical approaches (National Cancer Institute, n.d.-a).

Figure 9 presents an example of brain magnetic resonance images used in tumor assessment. The figure illustrates

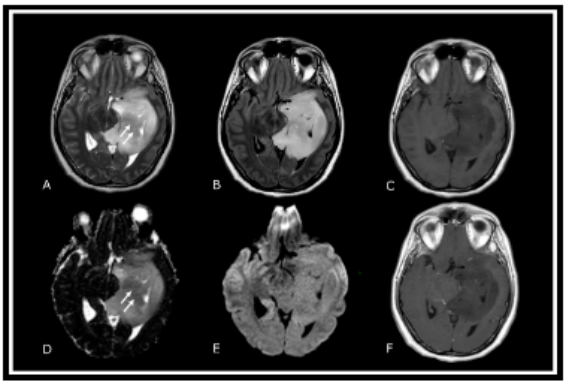

Figure 9: Example of magnetic resonance imaging used in brain tumor assessment and follow-up

how MRI can reveal the lesion and its morphological evolution through imaging, serving as a visual basis for clinical interpretation and, in the context of this work, for subsequent mathematical modeling of tumor regression (National Cancer Institute, n.d.-b).

Mathematical Modeling of Tumor Growth and Regression

A natural starting point for the present study is the classical Gompertz model, which became one of the best-known mathematical descriptions of tumor kinetics because it represents a fast initial phase followed by progressive deceleration as the lesion approaches biological constraints imposed by the host environment (Benzekry *et al.,* 2014; Laird, 1964).

In its differential form, the Gompertz model may be written as

$dV/dt=\alpha V\ln(K/V)$,

where V(t) is the tumor volume, $\alpha>0$ is a kinetic parameter, and K is the carrying capacity. Equation (1) is appropriate for untreated or freely evolving tumor growth, but this is not exactly the situation addressed in the present work. Here, the central phenomenon is not unrestricted growth, but geometric regression observed in sequential magnetic resonance images after therapy.

For this reason, the Gompertz formulation is adopted only as a conceptual basis. Its main limitation in the present context is that the variable V(t) represents only global tumor volume, whereas magnetic resonance imaging also reveals directional geometric changes, such as nonuniform shrinkage along different anatomical axes. Thus, instead of keeping a purely volumetric law, the model must be reformulated in terms of geometric quantities directly associated with the lesion observed in MRI.

To make this transition explicit, we first rewrite the volume in terms of a characteristic linear dimension. If the tumor were approximately spherical, one could write

$V(t)=4/3\ \pi r^3\ (t)$,

where r(t) is the effective radius. Differentiating both sides with respect to time,

$dV/dt=d/dt\ (4/3\ \pi r^3\ )$.

Since $4/3\ \pi$ is constant, it may be placed outside the derivative:

$dV/dt=4/3\ \pi\ d/dt(r^3)$.

Applying the chain rule,

$d/dt(r^3)=3r^2\ dr/dt$,

and therefore

$dV/dt=4\pi r^2\ dr/dt$.

Substituting (6) into the Gompertz equation (1), one obtains

$4\pi r^2\ dr/dt=\alpha(4/3\ \pi r^3\ )\ln(K/(4/3\ \pi r^3\ ))$.

Dividing both sides by $4\pi r^2$,

$dr/dt=\alpha/3\ r\ln(K/(4/3\ \pi r^3\ ))$.

Equation (8) already shows an important idea: a volumetric model can be reformulated as a geometric model. However, for the present study, even this spherical description remains insufficient, because medulloblastoma regression observed in MRI is not expected to be perfectly isotropic. A more realistic simplification is therefore to represent the tumor as an ellipsoid.

The ellipsoidal volume is written as

$V(t)=4/3\ \pi a(t)b(t)c(t)$,

where a(t), b(t), and c(t) are the semi-axes of the lesion along three orthogonal directions extracted from the magnetic resonance images.

We now differentiate (9) with respect to time. Since $4/3\ \pi$ is constant,

$dV/dt=4/3\ \pi\ d/dt\ [a(t)b(t)c(t)]$.

The derivative of a product of three functions is obtained by repeated application of the product rule:

$d/dt\ [abc]=bc\ da/dt+ac\ db/dt+ab\ dc/dt$.

Therefore,

$dV/dt=4/3\ \pi(bc\ da/dt+ac\ db/dt+ab\ dc/dt)$.

At this point, instead of forcing the original Gompertz law directly onto V(t), we introduce a regression-oriented hypothesis consistent with post-therapy MRI follow-up. We assume that each semi-axis decreases proportionally to its current magnitude, which leads to a first-order directional decay law:

$da/dt=-\lambda_1\ a$,

$db/dt=-\lambda_2\ b$,

$dc/dt=-\lambda_3\ c$,

where λ_1, λ_2, and λ_3 are nonnegative regression coefficients. This assumption is mathematically simple, physically interpretable, and directly compatible with sequential imaging data.

Substituting (13), (14), and (15) into (12), we obtain

$dV/dt=4/3\ \pi[bc(-\lambda_1\ a)+ac(-\lambda_2\ b)+ab(-\lambda_3\ c)]$.

Rearranging the terms,

$dV/dt=4/3\ \pi[-\lambda\lambda_1\ abc-\lambda_2\ abc-\lambda_3\ abc]$.

Factoring out the common product abc,

$dV/dt=4/3\ \pi abc[-(\lambda\lambda_1+\lambda_2+\lambda_3)]$.

Using (9), namely

$4/3\ \pi abc=V$,

we finally obtain

$dV/dt=-(\lambda\lambda_1+\lambda_2+\lambda_3)V$.

Equation (20) is the macroscopic volumetric law derived from the directional regression of the three semi-axes. If we define

$\Lambda=\lambda\lambda_1+\lambda_2+\lambda_3$,

then (20) becomes

$dV/dt=-\Lambda V$.

This equation is formally simpler than the Gompertz law, but it is more appropriate for the present purpose because it describes regression rather than growth and emerges directly from geometric assumptions consistent with MRI follow-up.

We now solve the system for each semi-axis. Starting from (13),

$da/dt=-\lambda_1\ a$,

we separate variables:

$1/a\ da=-\lambda_1\ dt$.

Integrating both sides,

$\int 1/a\ da=\int-\lambda_1\ dt$,

which yields

$\ln|a| = -\lambda_1 t + C_1$.
Exponentiating both sides,
$a(t) = A_1 e^{(-\lambda_1 t)}$,
where $A_1 = e^{(C_1)}$. Using the initial condition $a(0) = a_0$,
$a_0 = A_1$,
and therefore
$a(t) = a_0 e^{(-\lambda_1 t)}$.
By the same procedure,
$b(t) = b_0 e^{(-\lambda_2 t)}$,
and
$c(t) = c_0 e^{(-\lambda_3 t)}$.
Substituting (29), (30), and (31) into the ellipsoidal volume formula (9), we obtain

$$V(t) = \frac{4}{3}\pi\left(a_0 e^{-\lambda_1 t}\right)\left(b_0 e^{-\lambda_2 t}\right)\left(c_0 e^{-\lambda_3 t}\right).$$

Grouping the constant factors,

$$V(t) = \frac{4}{3}\pi a_0 b_0 c_0 \left(e^{-\lambda_1 t} e^{-\lambda_2 t} e^{-\lambda_3 t}\right).$$

Using the exponential property $e^x e^y = e^{(x+y)}$,

$$V(t) = \frac{4}{3}\pi a_0 b_0 c_0\, e^{-(\lambda_1+\lambda_2+\lambda_3)t}.$$

If the initial tumor volume is defined as
$V_0 = 4/3\ \pi a_0\ b_0\ c_0$,
then the final model may be written in the compact form
$V(t) = V_0 e^{(-\Lambda t)}$.

Thus, the proposed formalism is inspired by the classical tumor-growth literature, but it is deliberately reformulated to suit the present problem: treatment-induced geometric regression in pediatric medulloblastoma observed through magnetic resonance imaging. In practical terms, once a published clinical case with sequential MRI scans is selected, the tumor dimensions measured in each image may be associated with a(t), b(t), and c(t), allowing the regression process to be interpreted quantitatively through equations (29)–(36). This approach preserves the mathematical spirit of the classical models while adapting the formalism to a clinically meaningful imaging-based framework (Benzekry *et al.,* 2014; Laird, 1964; Liu *et al.,* 2022).

RESULTS AND DISCUSSION

Selection of the Clinical Case from the Literature

The selected reference article by Rojas *et al.* (2024) reports the clinical, radiological, and pathological course of a 2-year-old male diagnosed with pediatric medulloblastoma, emphasizing the role of magnetic resonance imaging in identifying the posterior fossa lesion, its mass effect, postoperative changes, and residual disease (Rojas *et al.,* 2024). In the present study, this case will be used as the clinical-imaging basis for the proposed mathematical formalism. After extracting the geometric

Table 1: Main clinical and imaging parameters reported by Rojas *et al.* (2024)

Parameter	Reported information
Patient age	2 years
Sex	Male
Tumor type	Desmoplastic nodular medulloblastoma
Main location	Right pontocerebellar angle / internal auditory canal
Initial imaging modality	Brain MRI
Relevant MRI findings	Mass effect, brainstem displacement, fourth ventricle collapse
Hydrocephalus	Acute supratentorial hydrocephalus
Surgical procedure	Craniotomy with lesion resection
Postoperative MRI	Residual extra-axial mass and surgical changes
Adjuvant treatment	Fractionated radiotherapy indicated
Detailed dose data	Not reported

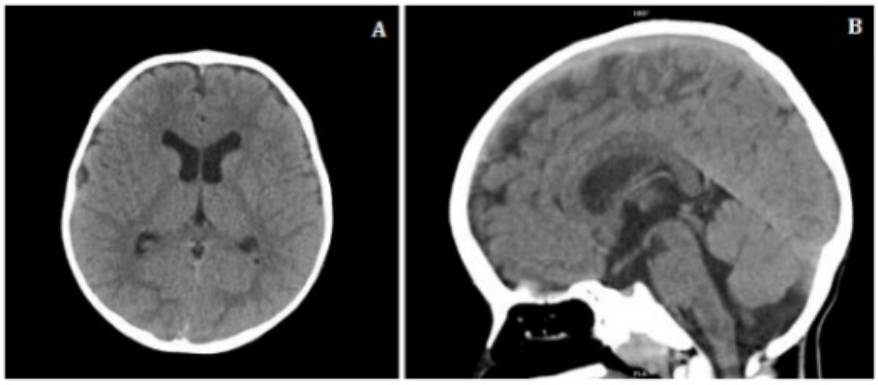

Figure 10: Baseline cranial computed tomography of a 2-year-old male patient. Panel A shows the axial view and Panel B the sagittal view. The examination demonstrates preserved gray–white matter differentiation, no supratentorial parenchymal alteration, normal ventricular morphology, absence of extra-axial collections, and a posterior fossa appearance without evident gross structural distortion in this section

information visible in the MRI figures, the tumor evolution will be translated into mathematical parameters and interpreted through the differential model derived in the previous subsection. It should be noted, however, that this paper does not provide a detailed proton therapy dosimetric dataset, so the mathematical analysis will be primarily image-based rather than dose-response based (Rojas *et al.,* 2024).

From a mathematical perspective, the image shown in Figure 10 may be interpreted as a spatial domain $\Omega \subset R^3$, representing the intracranial volume occupied by normal and pathological structures. In a first approximation, the radiological intensity may be described as a scalar field

$I=I(x,y,z)$,

where I denotes the tomographic intensity distribution and (x,y,z) are the spatial coordinates of the image.

If the lesion is later identified inside a specific subregion $\Omega_T \subset \Omega$, then the tumor may be geometrically represented as a bounded subset of the cranial domain. In simplified form, its volume can be defined by

$$V_T = \iiint_{\Omega_T} dV.$$

As a first geometric approximation, the tumor may be modeled as a sphere or ellipsoid. In the spherical case,

$V_T=4/3\ \pi r^3$,

where r is the equivalent tumor radius. In the more general ellipsoidal representation,

$V_T=4/3\ \pi abc$,

where a, b, and c are the semi-axes associated with the three principal anatomical directions.

Thus, even though Figure 7 does not yet provide the full magnetic resonance characterization of the lesion, it establishes the anatomical coordinate system and the geometric support needed for subsequent modeling. Once the lesion is visible in the MRI figures, the same formalism can be specialized by assigning values to a, b, and c, thereby allowing the tumor to be translated into a mathematically measurable object.

In this sense, the image is not interpreted merely as a visual clinical record, but as a spatially organized physical

Table 2: Main MRI parameters extracted from the preoperative lesion described by Rojas *et al.* (2024)

Parameter	Reported information
Patient age	2 years
Sex	Male
Imaging modality	Brain MRI
Acquisition planes	Axial and coronal
Scanner field strength	1.5 T
Reported sequences	TSE, T1, T2, susceptibility-sensitive sequence
Tumor location	Right cerebellopontine angle / internal auditory canal
Signal characteristics	T1 hypointense, heterogeneous T2 hyperintense
Additional signal feature	Peripheral intrinsic T1 hyperintensity suggestive of blood products
Enhancement pattern	Heterogeneous enhancement after contrast
Mass effect	Brainstem displacement and right cerebellar hemisphere compression
Ventricular effect	Near-complete obliteration of the fourth ventricle
Reported dimensions	40.7 × 56.9 × 33 mm
Approximate geometric model	Triaxial ellipsoid

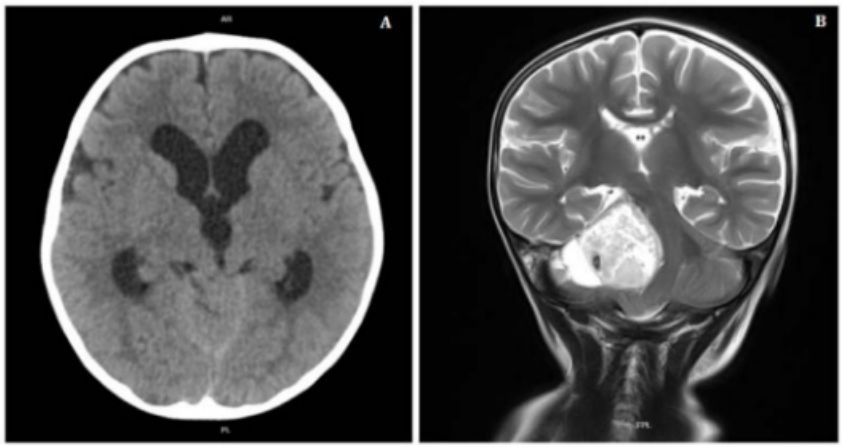

Figure 11: Preoperative neuroimaging of the pediatric medulloblastoma case. Panel A shows the axial image and Panel B the coronal MRI view, demonstrating a right posterior fossa lesion with marked mass effect, brainstem displacement, and fourth-ventricle compression

domain from which a tumor geometry can later be extracted and incorporated into the regression model.

The image shown in Figure 8 provides the first direct geometric representation of the lesion and therefore constitutes the natural starting point for mathematical formalization. From a spatial point of view, the tumor may be represented as a bounded subset

$\Omega_T \subset \Omega \subset R^3$,

where Ω denotes the intracranial domain and Ω_T the tumor region identified on MRI.

The radiological signal itself may be interpreted as a scalar field

$I=I(x,y,z)$,

with I representing the image intensity distribution and (x,y,z) the spatial coordinates. In practice, however, the present study is not focused on voxel-by-voxel signal modeling, but on the geometric evolution of the lesion. For this reason, the tumor is approximated by a triaxial ellipsoid.

Thus, its volume is defined by

$V(t)=4/3\ \pi a(t)b(t)c(t)$,

where a(t), b(t), and c(t) are the semi-axes associated with the three principal directions of the lesion.

Using the dimensions reported in the article,

$L_1=40.7$ "mm", $L_2=56.9$ "mm", $L_3=33.0$ "mm",

the corresponding semi-axes are

$a_0=40.7/2=20.35$ "mm",

$b_0=56.9/2=28.45$ "mm",

$c_0=33.0/2=16.50$ "mm".

Substituting these values into Equation (43), the initial tumor volume is

$V_0=4/3\ \pi(20.35)(28.45)(16.50)$.

Performing the algebra step by step,

$20.35\times28.45=579.9575$,

$579.9575\times16.50=9569.29875$,

thus

$V_0=4/3\ \pi\times9569.29875$.

Using

$4/3\ \pi\approx4.18879$,

one obtains

$V\_0\approx4.18879\times9569.29875$,

and therefore

$V_0\approx40083.8\ mm^3$.

Since

$1\ cm^3=1000\ mm^3$,

the initial lesion volume may also be written as

$V_0\approx40.08\ cm^3$.

To describe the evolution of this lesion over time, we assume that each semi-axis regresses continuously under treatment according to a first-order differential law:

$da/dt=-\lambda_1 a$,

$db/dt=-\lambda_2 b$,

$dc/dt=-\lambda_3 c$.

These equations state that the instantaneous variation of each geometric axis is proportional to its current size. The larger the axis, the greater its absolute reduction rate; as the lesion shrinks, the rate decreases proportionally.

We now solve Equation (57). Separating variables,

$1/a\,da=-\lambda_1\,dt$.

Integrating both sides,

$\int 1/a\,da=\int -\lambda_1\,dt$,

which gives

$\ln|a|=-\lambda_1 t+C_1$.

Exponentiating both sides,

$a(t)=A_1\ e^{(-\lambda_1 t)}$.

Using the initial condition $a(0)=a_0$,

$a_0=A_1$,

thus

$a(t)=a_0\ e^{(-\lambda_1 t)}$.

By the same procedure,

$b(t)=b_0\ e^{(-\lambda_2 t)}$,

$c(t)=c_0\ e^{(-\lambda_3 t)}$.

Substituting these expressions into the ellipsoidal volume formula,

$V(t)=4/3\ \pi(a_0\ e^{(-\lambda 1\ t)})(b_0\ e^{(-\lambda_2 t)})(c_0\ e^{(-\lambda_3 t)})$.

Grouping constants and exponentials,

$$V(t)=\frac{4}{3}\pi a_0 b_0 c_0\ e^{-(\lambda_1+\lambda_2+\lambda_3)t}.$$

Since

$V_0=4/3\ \pi a_0\ b_0\ c_0$,

the regression model becomes

$V(t)=V_0\ e^{-(\lambda\_1+\lambda\_2+\lambda\_3)t}$.

Defining

$\Lambda=\lambda_1+\lambda_2+\lambda_3$,

the final compact form is

$V(t)=V_0\ e^{-\Lambda t}$.

Differentiating Equation (71) with respect to time,

$dV/dt=d/dt\ (V_0\ e^{-\Lambda t})$,

and since V_0 is constant,

$dV/dt=V_0\ d/dt\ (e^{-\Lambda t})$.

Applying the chain rule,

$d/dt\ (e^{-\Lambda t})=-\Lambda e^{-\Lambda t}$,

thus

$dV/dt=-\Lambda V_0\ e^{-\Lambda t}$.

Since $V(t)=V_0\ e^{-\Lambda t}$,

$dV/dt=-\Lambda V$.

Therefore, the lesion represented in Figure 11 is mathematically translated into an initial ellipsoidal configuration of approximately 40.08 cm^3, whose subsequent response may be described through an exponential geometric regression law. Once later MRI images are inserted into the analysis, the same formalism can be reused to estimate λ_1, λ_2, and λ_3, compare different stages of the disease, and determine whether the regression is isotropic or anisotropic.

A contrast-enhanced postoperative cervical spine MRI was subsequently performed to investigate possible neuraxial extension and postsurgical changes. According to Rojas *et al.* (2024), this examination showed nonspecific edema in the nuchal region and right side of the neck, fluid collection adjacent to the surgical site, and no evidence of secondary neoplastic disease in the cervical spine, which makes this image particularly useful as a post-resection reference for mathematical comparison with the preoperative state.

Table 3: Main parameters associated with the postoperative cervical spine MRI reported by Rojas *et al.*

Parameter	Reported information
Clinical stage	Postsurgical imaging
Imaging modality	Contrast-enhanced cervical spine MRI
Planes shown	Sagittal and coronal
Scanner field strength	1.5 T
Reported sequences	SE, TSE, FE, or IR
Main postsurgical finding	Nonspecific soft-tissue edema
Regional involvement	Nuchal region and right side of the neck
Fluid collection	Present adjacent to the surgical site
Residual mass	Partially visualized right peritrochlear cistern mass
Morphology of residual lesion	Cystic and solid components
Metastatic / secondary disease	Not identified in this examination
Detailed radiotherapy dose	Not reported in the case description
Detailed fractionation scheme	Not reported in the case description
Mathematical role in this work	Postoperative comparison state

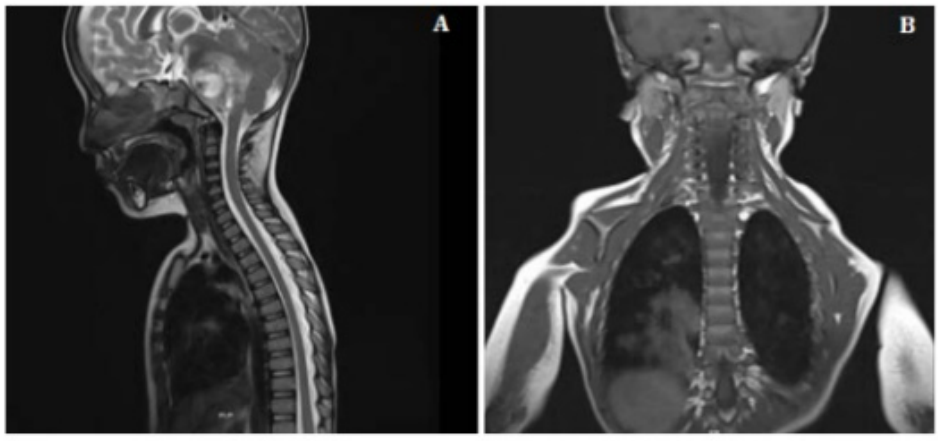

Figure 12: Postoperative contrast-enhanced cervical spine MRI. Panel A shows the sagittal view and Panel B the coronal view, demonstrating postsurgical soft-tissue changes, adjacent fluid collection, and partial visualization of a residual mass on the right side

From a mathematical point of view, the postoperative image shown in Figure 12 represents a new geometric state of the disease after surgical intervention. If the preoperative lesion is denoted by the domain

$\Omega_T^{(0)} \subset \Omega$,

and the postoperative residual lesion by

$\Omega_T^{(1)} \subset \Omega$,

then the corresponding tumor volumes may be written as

$$a_{t,1} = \frac{f(Y_t|S_t = i)\pi_i}{\sum_{j=1} f(Y_t|S_t = j)\pi_j} = [(Y_t|S_t = i)\pi_i]$$

and

$$V_1 = \iiint_{\Omega_T^{(1)}} dV.$$

In the present formalism, both states are approximated by triaxial ellipsoids. Therefore,

$V_0=4/3\ \pi a_0\ b_0\ c_0$

and

$V_1=4/3\ \pi a_1\ b_1\ c_1$,

where (a_0,b_0,c_0) are the preoperative semi-axes and (a_1,b_1,c_1) are the postoperative semi-axes inferred from the residual lesion.

The preoperative model derived in the previous subsection assumed first-order directional regression:

$da/dt=-\lambda_1\ a$,

$db/dt=-\lambda_2\ b$,

$dc/dt=-\lambda_3\ c$.

The corresponding solutions are

$a(t)=a_0\ e^{(-\lambda_1\ t)}$,

$b(t)=b_0\ e^{(-\lambda_2\ t)}$,

$c(t)=c_0\ e^{(-\lambda_3\ t)}$.

Substituting these expressions into the ellipsoidal volume formula,

$V(t)=4/3\ \pi(a_0\ e^{(-\lambda_1\ t)})(b_0\ e^{(-\lambda_2\ t)})(c_0\ e^{(-\lambda_3\ t)})$.

Grouping the exponential factors,

$V(t)=4/3\ \pi a_0\ b_0\ c_0\ e^{(-(\lambda_1+\lambda_2+\lambda_3)t)}$.

Since

$V_0=4/3\ \pi a_0\ b_0\ c_0$,

one obtains the compact law

$V(t)=V_0\, e^{(-\Lambda t)}$,
with
$\Lambda=\lambda_1+\lambda_2+\lambda_3$.
Now, let $t=t_1$ denote the postoperative imaging time associated with Figure 9. Then
$V_1=V(t_1)=V_0\, e^{(-\Lambda t_1)}$.
To isolate the effective regression coefficient Λ, divide both sides of Equation (96) by V_0:
$V_1/V_0=e^{(-\Lambda t_1)}$.
Applying the natural logarithm to both sides,
$\ln(V_1/V_0)=\ln(e^{(-\Lambda t_1)})$.
Since $\ln(e^x)=x$,
$\ln(V_1/V_0)=-\Lambda t_1$.
Thus,
$\Lambda=-1/t_1\ \ln(V_1/V_0)$.
Equation (100) is fundamental because it allows the effective regression rate to be estimated directly from two image-defined states: the preoperative configuration and the postoperative residual configuration.
It is also useful to define the residual volumetric fraction:
$R_V=V_1/V_0$,
and the volumetric reduction fraction:
$\eta_V=1-V_1/V_0$.
If the regression were isotropic, then
$\lambda_1=\lambda_2=\lambda_3=\lambda$,
which implies
$\Lambda=3\lambda$.
In this special case,
$a(t)=a_0\, e^{(-\lambda t)}$, $b(t)=b_0\, e^{(-\lambda t)}$, $c(t)=c_0\, e^{(-\lambda t)}$,
and therefore
$V(t)=4/3\ \pi a_0\, b_0\, c_0\, e^{(-3\lambda t)}=V_0\, e^{(-3\lambda t)}$.
Hence,
$\lambda=-1/(3t_1)\ \ln(V_1/V_0)$.

On the other hand, if the postoperative image suggests asymmetric residual geometry, then the regression must be treated as anisotropic. In that case, directional ratios may be introduced:
$\varrho_a=a_1/a_0$, $\varrho_b=b_1/b_0$, $\varrho_c=c_1/c_0$.
Using the axis solutions,
$a_1=a_0\, e^{(-\lambda_1 t_1)}$, $b_1=b_0\, e^{(-\lambda_2 t_1)}$, $c_1=c_0\, e^{(-\lambda_3 t_1)}$,
we obtain
$\varrho_a=e^{(-\lambda_1 t_1)}$, $\varrho_b=e^{(-\lambda_2 t_1)}$, $\varrho_c=e^{(-\lambda_3 t_1)}$.
Taking logarithms,
$\lambda_1=-1/t_1\ \ln(\varrho_a)$,
$\lambda_2=-1/t_1\ \ln(\varrho_b)$,
$\lambda_3=-1/t_1\ \ln(\varrho_c)$.
Therefore, once the residual lesion dimensions are estimated from Figure 9, the postoperative image can be used not only to calculate a new tumor volume V_1, but also to determine whether the regression pattern is isotropic or direction-dependent. In this way, the image ceases to be only a postsurgical radiological record and becomes a mathematically interpretable state in the dynamical evolution of the lesion. The paper reports that this postoperative cervical MRI showed soft-tissue edema, adjacent fluid collection, partial residual mass visualization, and no secondary neoplastic disease in the cervical spine, which supports its use here as a postoperative comparison frame rather than as evidence of neuraxial metastatic spread.
A thoracic spine MRI with gadolinium was then performed as part of the metastatic assessment. According to Rojas *et al.* (2024), this examination was essentially within normal limits, with no lesions suggestive of secondary neoplastic disease, making it useful in this study as a mathematical reference state compatible with absence of thoracic spinal dissemination.

Table 4: Main parameters associated with the thoracic spine MRI reported by Rojas *et al.* (2024).

Parameter	**Reported information**
Clinical stage	Postsurgical / staging evaluation
Imaging modality	Thoracic spine MRI with gadolinium
Planes shown	Coronal and sagittal
Scanner field strength	1.5 T
Reported sequences	SE, TSE, FE, or IR
Bone marrow signal	Normal
Vertebral bodies	Normal height, alignment, and configuration
Intervertebral discs	Normal height
Posterior elements	Normal
Spinal canal caliber	Normal
Neural foramina caliber	Normal
Spinal cord	Normal thickness and signal intensity
Post-gadolinium enhancement	No abnormal enhancement detected
Paravertebral soft tissues	No masses identified
Spinal canal masses	Not identified
Leptomeningeal / dural enhancement	Not identified
Detailed radiotherapy dose	Not reported
Detailed fractionation scheme	Not reported
Mathematical role in this work	Reference state without thoracic metastatic spread

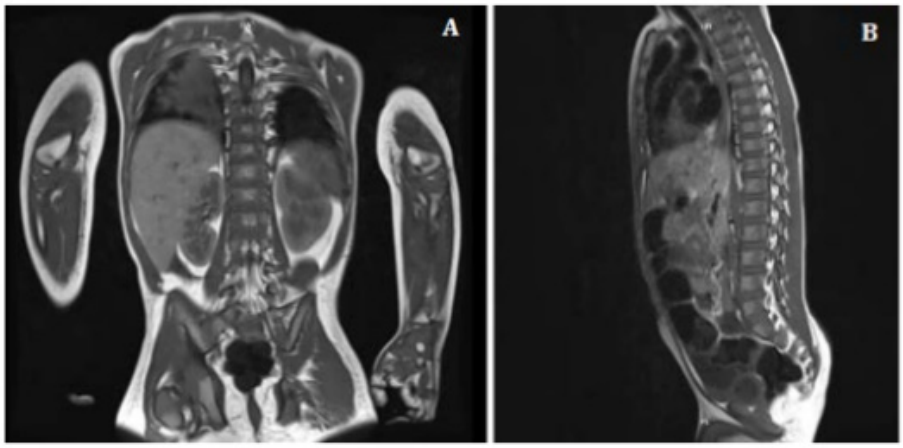

Figure 13: Thoracic spine MRI with gadolinium. Panel A shows the coronal view and Panel B the sagittal view. The examination demonstrates normal vertebral alignment, preserved spinal canal caliber, no abnormal enhancement, and no lesions suggestive of thoracic metastatic dissemination

From a mathematical perspective, Figure 13 is important not because it reveals a measurable thoracic metastatic lesion, but because it defines a limiting case in which the pathological volumetric contribution in the thoracic spinal domain is approximately null. Let

$\Omega_S \subset R^3$

denote the thoracic spinal domain investigated by MRI, and let

$\Omega_M \subset \Omega_S$

represent a hypothetical metastatic subdomain.

If metastatic disease were present, its volume could be defined as

$V_M = \iiint_{(\Omega M)} {}^{dV}$.

However, because the reported examination did not identify thoracic lesions suggestive of metastasis, the present image is modeled under the approximation

$\Omega_M \approx \varnothing$,

and therefore

$V_M \approx 0$.

This result may also be interpreted through an indicator function. Define

$$\chi_M(x,y,z) = \begin{cases} 1, & (x,y,z) \in \Omega_M, \\ 0, & (x,y,z) \notin \Omega_M. \end{cases}$$

Then the metastatic volume may be rewritten as

$$V_M = \iiint_{\Omega_S} \chi_M(x,y,z)\, dV.$$

Since no metastatic focus is identified,

$\chi_M(x,y,z) \approx 0$ "in " Ω_S,

which again leads to

$V_M \approx 0$.

To connect this image with the previous differential formalism, let the primary posterior fossa lesion volume be denoted by $V_T(t)$, and let the thoracic metastatic component be denoted by $V_M(t)$. The total measurable tumor burden may then be written as

$V_{tot}(t) = V_T(t) + V_M(t)$.

Because the thoracic MRI does not reveal metastatic dissemination,

$V_M(t_4) \approx 0$,

at the imaging time associated with Figure 10, and thus

$V_{tot}(t_4) \approx V_T(t_4)$.

This is useful because it means that, at this stage, the dynamical burden of disease remains dominated by the primary intracranial lesion rather than by neuraxial thoracic spread.

If one wishes to describe the possible emergence of metastatic disease in a general form, a first-order source equation may be introduced:

$(dV_M)/dt = \sigma(t) - \mu V_M$,

where $\sigma(t)$ represents the effective rate of metastatic seeding and μ represents clearance or suppression of measurable metastatic burden.

In the present image-based situation, the thoracic MRI suggests absence of measurable metastatic seeding, so that

$\sigma(t_4) \approx 0$.

Substituting this approximation into Equation (126),

$(dV_M)/dt \approx -\mu V_M$.

Separating variables,

$1/V_M \, dV_M = -\mu \, dt$.

Integrating both sides,

$\int 1/V_M \, dV_M = \int -\mu \, dt$,

we obtain

$\ln|V_M| = -\mu t + C$.

Exponentiating,

$V_M(t) = C_0 e^{(-\mu t)}$.

If the initial measurable thoracic metastatic burden is negligible, that is,

$V_M(0) \approx 0$,

then the physically consistent interpretation is

$V_M(t) \approx 0$

throughout the interval represented by this staging study. Therefore, Equation (123) reduces to

$V_{tot}(t) \approx V_T(t)$,

which preserves the validity of the previous intracranial regression model:

$V_T(t) = V_0 e^{(-\Lambda t)}$.

Differentiating with respect to time,

$(dV_T)/dt=d/dt\ (V_0\ e^{(-\Lambda t)})$.
Since V_0 is constant,
$(dV_T)/dt=V_0\ \ d/dt\ (e^{(-\Lambda t)})$.
Applying the chain rule,
$d/dt\ (e^{(-\Lambda t)})=-\Lambda e^{(-\Lambda t)}$,
thus
$(dV_T)/dt=-\Lambda V_0\ e^{(-\Lambda t)}$.
Since $V_T\ (t)=V_0\ e^{(-\Lambda t)}$,
$(dV_T)/dt=-\Lambda V_T$.
Hence, the role of Figure 10 in the present formalism is to establish a mathematically relevant negative result: the thoracic spinal contribution to tumor burden is negligible in this case. This finding constrains the model by indicating that the dominant measurable disease remains localized to the primary intracranial compartment, allowing the subsequent quantitative interpretation to remain focused on geometric regression of the main lesion.
A chest radiograph was later obtained during the clinical course because of acute respiratory infection. Although this image is not part of the direct neuro-oncological geometric follow-up, it is still relevant in the present study because it documents systemic clinical complications during the patient's evolution and provides an additional state of observation outside the central nervous system compartment.

Table 5: Main parameters associated with the chest radiography reported by Rojas *et al.* (2024)

Parameter	Reported information
Clinical stage	Intercurrent systemic complication
Imaging modality	Chest radiography
Views shown	Anteroposterior views
Main clinical indication	Acute respiratory infection
Cardiophrenic silhouette	Preserved
Pulmonary vascularity	Preserved
Mediastinum	Without alteration
Peribronchovascular interstitium	Thickened
Pulmonary consolidation	Multilobar consolidation in Panel A
Pneumothorax	Right pneumothorax in Panel B
Airway device	Endotracheal tube with distal tip at T3
Detailed radiotherapy dose	Not reported
Detailed fractionation scheme	Not reported
Mathematical role in this work	Extracranial clinical state outside the primary tumor compartment

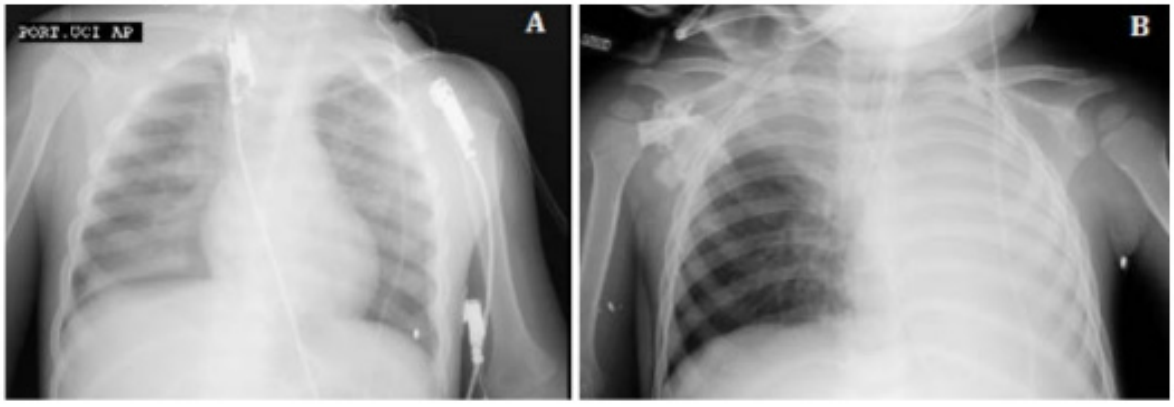

Figure 14: Chest radiography obtained during the clinical course. Panel A shows multilobar pulmonary consolidation, while Panel B demonstrates right pneumothorax and the position of the endotracheal tube

From a mathematical point of view, Figure 14 does not directly describe the intracranial tumor geometry, but it can be incorporated into the global clinical model as an auxiliary extracranial state variable. Let the total disease-related state of the patient be represented by
$S(t)=S_T\ (t)+S_C\ (t)$,
where $S_T\ (t)$ denotes the tumor-related component and $S_C\ (t)$ denotes the systemic clinical complication component. The tumor contribution may still be represented through the volumetric law previously derived:
$V_T\ (t)=V_0\ e^{(-\Lambda t)}$,
with
$(dV_T)/dt=-\Lambda V_T$.
However, the chest radiograph suggests that the patient also presents a non-neoplastic pulmonary burden. Let this extracranial pulmonary complication be represented by a scalar variable
$P(t)\geq 0$,

where P(t) is a simplified measure of respiratory compromise associated with consolidation, pneumothorax, or both.

A minimal first-order model for the pulmonary burden may be written as

$dP/dt=\alpha_P-\beta_P P$,

where α_P represents the effective rate of clinical aggravation and β_P represents the effective rate of resolution under support measures.

To solve Equation (146), we first rewrite it as

$dP/dt+\beta_P P=\alpha_P$.

This is a linear first-order differential equation. Its integrating factor is

$\mu(t)=e^{(\int \beta_P dt)}=e^{(\beta_P t)}$.

Multiplying the entire equation by $e^{(\beta_P t)}$,

$e^{(\beta_P t)} dP/dt+\beta_P e^{(\beta_P t)} P=\alpha_P e^{(\beta_P t)}$.

The left-hand side is the derivative of a product:

$d/dt (Pe^{(\beta_P t)})=\alpha_P e^{(\beta_P t)}$.

Integrating both sides,

$\int d/dt (Pe^{(\beta_P t)})dt=\int \alpha_P e^{(\beta_P t)} dt$,

we obtain

$Pe^{(\beta_P t)}=\alpha_P/\beta_P e^{(\beta_P t)}+C$.

Dividing both sides by e^(β_P t),

$P(t)=\alpha_P/\beta_P +Ce^{(\beta_P t)}$.

If the initial pulmonary burden is $P(0)=P_0$, then

$P_0=\alpha_P/\beta_P +C$,

so that

$C=P_0-\alpha_P/\beta_P$.

Hence,

$P(t)=\alpha_P/\beta_P +(P_0-\alpha_P/\beta_P) e^{(\beta_P t)}$.

Equation (156) shows that the respiratory complication evolves toward an equilibrium level α_P/β_P. In the special case in which no new aggravating source remains active after treatment support, one may set

$\alpha_P=0$,

and Equation (156) reduces to

$P(t)=P_0 e^{(\beta_P t)}$.

Differentiating,

$dP/dt=-\beta_P P$.

A coupled clinical descriptor may then be introduced:

$\Phi(t)=w_T V_T (t)+w_P P(t)$,

where w_T and w_P are weighting factors associated with tumor burden and pulmonary complication burden, respectively.

Differentiating Φ(t) with respect to time,

$d\Phi/dt=w_T (dV_T)/dt+w_P dP/dt$.

Substituting the governing equations,

$d\Phi/dt=w_T (-\Lambda V_T)+w_P (\alpha_P-\beta_P P)$.

Therefore,

$d\Phi/dt=-w_T \Lambda V_T+w_P \alpha_P-w_P \beta_P P$.

This expression is important because it shows that the global clinical evolution of the patient cannot always be reduced to tumor regression alone. Even if the intracranial lesion follows a decreasing law, extracranial complications may transiently increase the overall burden of disease.

Thus, Figure 11 plays a complementary role in the mathematical interpretation of the case: it does not redefine the primary tumor geometry, but it adds an auxiliary dynamical variable associated with systemic clinical deterioration. In this framework, the chest radiograph is interpreted not as part of the direct medulloblastoma volumetric model, but as an additional clinical state capable of interacting with the overall trajectory of the patient.

A postoperative contrast-enhanced brain MRI was obtained to evaluate the residual intracranial lesion after surgery. According to the case description, this examination is particularly important because it documents both postoperative structural changes and persistent residual tumor burden, thereby providing a key image for the transition from the preoperative state to the regression model developed in this study.

Table 6: Main parameters associated with the postoperative brain MRI reported in the selected clinical case (Rojas *et al.,* 2024).

Parameter	**Reported information**
Clinical stage	Postsurgical intracranial evaluation
Imaging modality	Contrast-enhanced brain MRI
Planes shown	Axial and coronal
Reported sequences	T1, T2, diffusion, FLAIR, and contrast-enhanced T1
Main postsurgical finding	Right occipital craniectomy changes
Parenchymal alteration	Encephalomalacia and gliosis in right cerebellar hemisphere
Residual lesion location	Prepontine, right pontocerebellar, and bulbar cisterns
Residual lesion character	Extra-axial characteristics
Signal on T1	Hypointense
Signal on T2	Heterogeneous
Contrast enhancement	Intense enhancement after contrast administration
Intracanalicular extension	Present
Mass effect	Moderate effect on the middle cerebellar peduncle
Meningeal enhancement	Supra- and infratentorial
Extra-axial collections	Fronto-parietal convexity, subdural morphology

Ventricular system	Moderately enlarged in the midline
Transependymal CSF migration	Not identified
Detailed radiotherapy dose	Not reported
Detailed fractionation scheme	Not reported
Mathematical role in this work	Residual intracranial tumor state after surgery

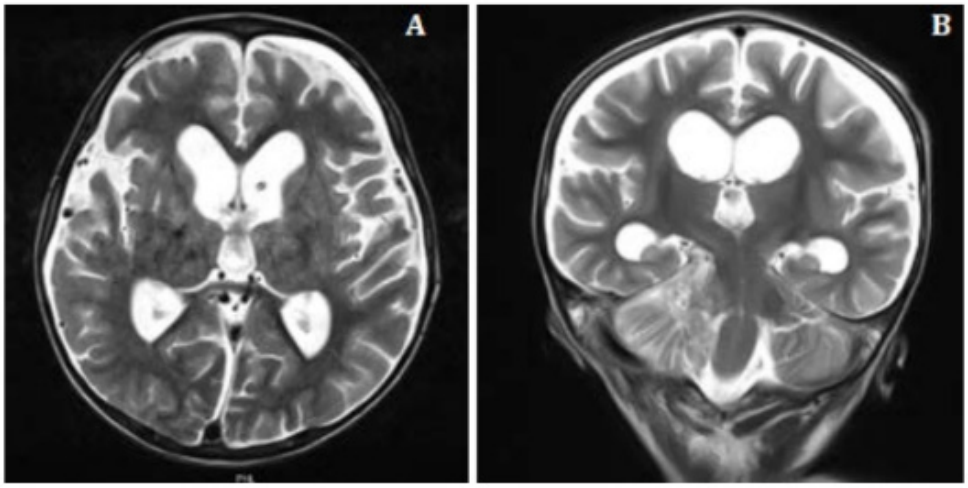

Figure 15: Postoperative contrast-enhanced brain MRI. Panel A shows the axial view and Panel B the coronal view, demonstrating postsurgical changes in the right posterior fossa and a residual extra-axial lesion with persistent mass effect and ventricular enlargement

From a mathematical perspective, Figure 15 represents a residual intracranial state that follows the preoperative configuration and the immediate postoperative comparison described previously. Let the initial preoperative lesion be associated with the volume

$V_0=4/3\ \pi a_0\ b_0\ c_0$,

and let the residual postoperative lesion visible in Figure 12 be represented by

$V_2=4/3\ \pi a_2\ b_2\ c_2$,

where a_2, b_2, and c_2 are the semi-axes of the residual lesion inferred from the postoperative MRI.

The evolution proposed in this work assumes that each principal dimension of the lesion obeys a first-order directional regression law:

$da/dt=-\lambda_1\ a$,

$db/dt=-\lambda_2\ b$,

$dc/dt=-\lambda_3\ c$.

Separating variables in the first equation,

$1/a\,da=-\lambda_1\,dt$,

and integrating both sides,

$\int 1/a\,da=\int -\lambda_1\,dt$,

we obtain

$\ln|a|=-\lambda_1\ t+C_1$.

Exponentiating,

$a(t)=A_1\ e^{(-\lambda_1\ t)}$.

Using the initial condition a(0)=a_0,

$a(t)=a_0\ e^{(-\lambda_1\ t)}$.

By the same procedure,

$b(t)=b_0\ e^{(-\lambda_2\ t)}$,

$c(t)=c_0\ e^{(-\lambda_3\ t)}$.

Substituting these expressions into the ellipsoidal volume formula,

$V(t)=4/3\ \pi(a_0\ e^{(-\lambda_1\ t)})(b_0\ e^{(-\lambda_2\ t)})(c_0\ e^{(-\lambda_3\ t)})$.

Grouping the exponential factors,

$V(t)=4/3\ \pi a_0\ b_0\ c_0\ e^{(-(\lambda_1+\lambda_2+\lambda_3)t)}$.

Since

$V_0=4/3\ \pi a_0\ b_0\ c_0$,

the residual volume law becomes

$V(t)=V_0\ e^{(-\Lambda t)}$,

with

$\Lambda=\lambda_1+\lambda_2+\lambda_3$.

Let t=t_2 denote the time associated with the MRI shown in Figure 12. Then

$V_2=V(t_2)=V_0\ e^{(-\Lambda t_2)}$.

Dividing both sides of Equation (181) by V_0,

$V_2/V_0=e^{(-\Lambda t2)}$.

Applying the natural logarithm,

$\ln(V_2/V_0)=\ln(e^{(-\Lambda t2)})$,

thus

$\ln(V_2/V_0)=-\Lambda t_2$,

and finally

$\Lambda=-1/t_2\ \ln(V_2/V_0)$.

Equation (185) is useful because it allows the effective regression rate to be estimated directly from the initial lesion and the residual postoperative lesion shown in the brain MRI.

A residual volumetric fraction may also be defined as

$R_2=V_2/V_0$,

while the corresponding reduction fraction is

$\eta_2=1-V_2/V_0$.

If one wishes to compare the immediate postoperative residual state with a previous postoperative state V_1, then

the relative interval behavior may be written as
$V_2/V_1 = e^{(-\Lambda(t_2 - t_1))}$.
Taking logarithms,
$\ln(V_2/V_1) = -\Lambda(t_2 - t_1)$,
which yields
$\Lambda = -1/(t_2 - t_1) \ln(V_2/V_1)$.
This form is particularly useful when sequential postoperative images are available, because it estimates the regression coefficient directly from two consecutive observed states without requiring continuous imaging.
The moderate ventricular enlargement described in the image may also be represented by an auxiliary state variable Q(t), associated with ventricular burden. A simple linear response model can be proposed:
$dQ/dt = \alpha_Q V(t) - \beta_Q Q$,
where α_Q represents the effect of lesion burden on ventricular alteration and β_Q represents the effective rate of recovery after decompression or clinical stabilization.
Substituting Equation (179) into Equation (191),
$dQ/dt + \beta_Q Q = \alpha_Q V_0 e^{(-\Lambda t)}$.
Multiplying both sides by the integrating factor $e^{(\beta_Q t)}$,
$e^{(\beta_Q t)} dQ/dt + \beta_Q e^{(\beta_Q t)} Q = \alpha_Q V_0 e^{((\beta_Q - \Lambda)t)}$.
The left-hand side is the derivative of a product:
$d/dt (Qe^{(\beta_Q t)}) = \alpha_Q V_0 e^{((\beta_Q - \Lambda)t)}$.
Integrating both sides,
$Qe^{(\beta_Q t)} = \alpha_Q V_0 \int e^{((\beta_Q - \Lambda)t)} dt + C$.
Assuming $\beta_Q \neq \Lambda$,
$Qe^{(\beta_Q t)} = \alpha_Q V_0 e^{((\beta_Q - \Lambda)t)}/(\beta_Q - \Lambda) + C$.
Dividing by $e^{(\beta_Q t)}$,
$Q(t) = (\alpha_Q V_0)/(\beta_Q - \Lambda) e^{(-\Lambda t)} + Ce^{(\beta_Q t)}$.
Therefore, the ventricular response may also be interpreted dynamically as a quantity driven by residual tumor burden and attenuated by postoperative recovery mechanisms.
In this way, Figure 15 is not only a descriptive postoperative image, but a mathematically meaningful residual state. It allows the lesion to be represented by a new ellipsoidal configuration, supports estimation of the effective regression coefficient, and permits the incorporation of secondary effects such as ventricular alteration into the overall dynamical framework of the case.

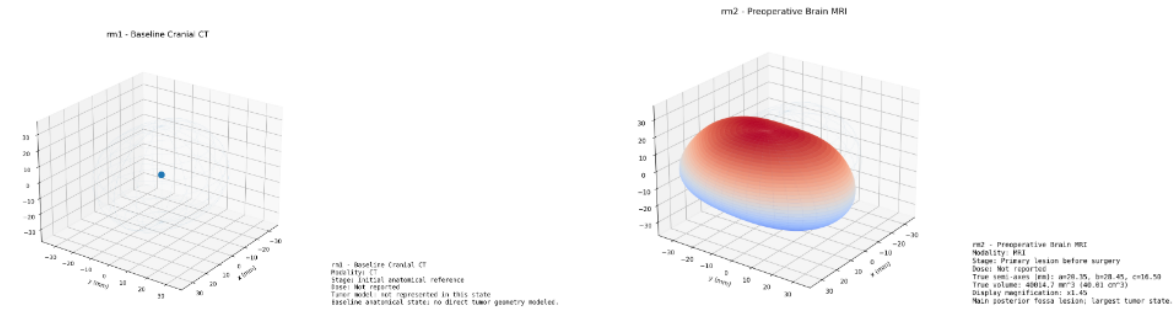

(a) Baseline cranial CT reference state. (b) Preoperative main tumor geometry.

Figure 16: (A) Baseline cranial CT reference state, (B) Preoperative main tumor geometry.

Initial Pair of Three-Dimensional Numerical Representations.
The first pair shown in Figure 16 establishes the transition from the initial anatomical reference state to the primary preoperative tumor geometry. While the baseline cranial CT does not yet provide a fully measurable tumor volume, the preoperative MRI-based reconstruction allows the lesion to be represented as a three-dimensional geometric object with defined semi-axes and computable volume.
This result illustrates the efficiency of the proposed mathematical formalism, since radiological information can be translated into geometric parameters and then converted into a numerical three-dimensional representation. In this way, the formalism provides not only an analytical description of tumor structure but also a visual computational model that facilitates clinical interpretation of lesion size and spatial organization.

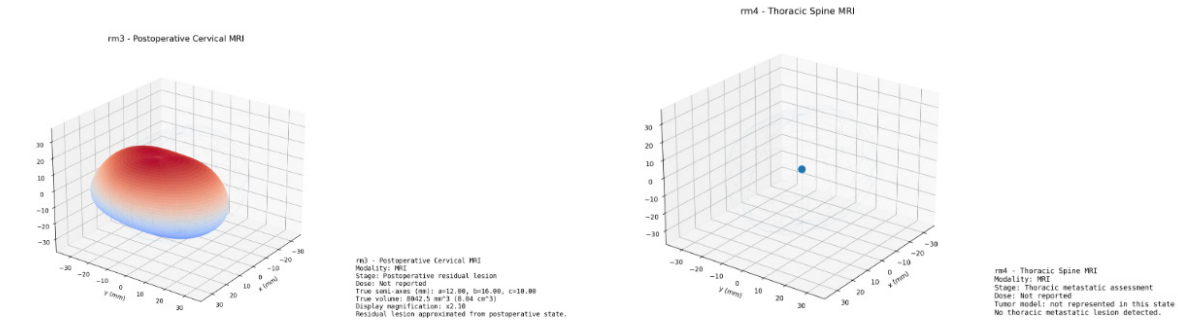

(a) Postoperative residual lesion. (b) Thoracic MRI without metastatic lesion.

Figure 17: (A) Postoperative residual lesion, (B) Thoracic MRI without metastatic lesion

Intermediate Postoperative and Staging Numerical Representations.

The second pair shown in Figure 17 represents an intermediate stage of the case, combining a postoperative residual lesion with a thoracic evaluation without detectable metastatic spread. Mathematically, this comparison is important because it distinguishes between residual intracranial tumor burden and extracranial states in which the pathological volumetric contribution is negligible.

Such a distinction reinforces the usefulness of the model, since the same mathematical framework can represent both positive tumor states and negative imaging states without measurable metastatic disease. Therefore, the formalism remains consistent across different clinical scenarios and supports a more structured interpretation of disease progression and localization.

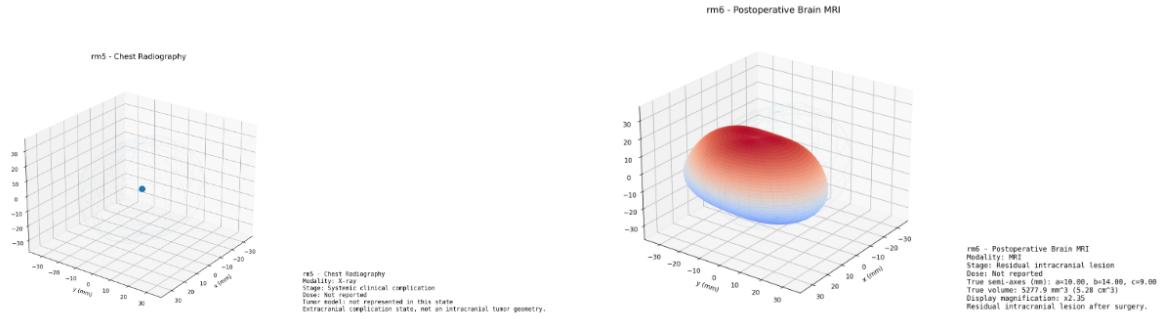

(a) Chest radiography as extracranial clinical state. (b) Residual intracranial postoperative tumor state.

Figure 18: (A) Chest radiography as extracranial clinical state, (B) Residual intracranial postoperative tumor state

Final Pair of Extracranial and Residual Intracranial Numerical Representations.

The final pair shown in Figure 18 combines an extracranial clinical complication state with a postoperative intracranial residual tumor state. This organization is relevant because it shows that the proposed mathematical formalism can distinguish between images directly associated with tumor geometry and images related to systemic clinical conditions that may influence the patient's overall course but do not redefine the primary tumor volume itself.

From a broader perspective, these three-dimensional reconstructions demonstrate that mathematical modeling can be effectively transformed into computational image generation. This capability is clinically meaningful because it allows tumor states reported in radiological examinations to be reinterpreted quantitatively, visually compared across time, and integrated into a consistent analytical framework. Consequently, the formalism proposed in this work may contribute to a more precise understanding of tumor geometry, residual disease, and clinical evolution in pediatric medulloblastoma.

CONCLUSION

This study proposed an original and interdisciplinary framework for the mathematical interpretation of pediatric medulloblastoma based on real clinical imaging data. Starting from classical models of tumor kinetics and advancing toward a regression-oriented geometric formalism, it was possible to construct a differential model capable of describing the three-dimensional evolution of the lesion through measurable parameters extracted from medical images. In this sense, the present work moved beyond a purely qualitative reading of radiological findings and demonstrated that mathematical language can be effectively incorporated into the clinical interpretation of tumor behavior.

One of the main contributions of this study lies in the fact that it addresses a clear gap in the literature. Although medical imaging plays a central role in diagnosis, follow-up, and therapeutic decision-making, the interpretation of these images is still predominantly descriptive in most clinical reports. By introducing differential equations, geometric simplification, and numerical simulation into the analysis of a real pediatric medulloblastoma case, this work shows that it is possible to build a more structured, quantitative, and reproducible framework for understanding lesion progression and regression over time.

Another important result is the demonstration that the proposed mathematical formalism is not restricted to theoretical derivation. Once implemented computationally in Python, the model was able to generate three-dimensional numerical representations of the tumor states, transforming analytical expressions into visual objects. This step is particularly relevant because it reinforces the practical value of the method: the same formalism that explains the temporal behavior of the lesion can also be used to reconstruct and visualize tumor geometry, thereby strengthening the bridge between applied mathematics, medical physics, and radiological interpretation.

From a scientific perspective, the study is innovative because it applies differential-equation-based reasoning to a clinical imaging problem that is rarely explored with this level of mathematical depth. Rather than treating medical images only as visual records, this work treats them as physically and geometrically structured domains from which dynamic information can be extracted. Such an approach opens the possibility of future applications in quantitative imaging, computational follow-up, model-based treatment assessment, and decision-support tools in pediatric neuro-oncology.

From a clinical perspective, the relevance of this work lies in showing that mathematical modeling may serve as a complementary instrument for interpreting tumor burden, residual disease, and geometric response after treatment. Even under the limitations of a case-report-based methodology and simplified geometric assumptions, the formalism proved capable of organizing the imaging findings into a coherent analytical structure. This indicates that mathematical approaches of this kind may contribute to more objective comparisons between different stages of disease evolution and may, in the future, support more refined image-based assessments in pediatric patients.

Therefore, this work should be understood not merely as an isolated theoretical exercise, but as a proof of concept for a new way of connecting mathematics and medicine. Its innovative character lies precisely in demonstrating that differential equations, geometric modeling, and numerical simulation can be used not only to describe abstract systems, but also to interpret real oncological images in a clinically meaningful way. In this sense, the present study contributes to the advancement of a still underexplored field and highlights the potential of mathematical formalism as a powerful auxiliary language for contemporary medical physics and pediatric oncology.

Finally, future investigations may expand this proposal by incorporating larger clinical datasets, more precise segmentation methods, anisotropic or deformable geometries, machine learning tools, and, when available, detailed dosimetric information. Such developments could further strengthen the predictive and interpretative power of the model and consolidate this line of research as a promising avenue for innovation in the quantitative study of pediatric brain tumors.

REFERENCES

Alcantara, J. H., Ornos, E. D. B., & Tantengco, O. A. G. (2023). Global trends, gaps, and future agenda in medulloblastoma research: A bibliometric analysis. *Child's Nervous System.* https://doi.org/10.1007/s00381-023-05969-2

Benzekry, S., Lamont, C., Beheshti, A., Tracz, A., Ebos, J. M. L., Hlatky, L., & Hahnfeldt, P. (2014). Classical mathematical models for description and prediction of experimental tumor growth. *PLOS Computational Biology, 10*(8), Article e1003800. https://doi.org/10.1371/journal.pcbi.1003800

Bray, F., Laversanne, M., Sung, H., Ferlay, J., Siegel, R. L., Soerjomataram, I., & Jemal, A. (2024). Global cancer statistics 2022: GLOBOCAN estimates of incidence and mortality worldwide for 36 cancers in 185 countries. *CA: A Cancer Journal for Clinicians, 74*(3), 229-263. https://doi.org/10.3322/caac.21834

CERN. (2014). Fifty years of quarks. https://home.web.cern.ch/news/news/physics/fifty-years-quarks

Cooney, T., Lindsay, H., Leary, S., & Wechsler-Reya, R. (2023). Current studies and future directions for medulloblastoma: A review from the Pacific Pediatric Neuro-Oncology Consortium (PNOC) disease working group. *Neoplasia, 35,* Article 100861. https://doi.org/10.1016/j.neo.2022.100861

Encyclopaedia Britannica. (n.d.-a). *Ernest Rutherford.* https://www.britannica.com/biography/Ernest-Rutherford

Encyclopaedia Britannica. (n.d.-b). *Rutherford model.* https://www.britannica.com/science/Rutherford-model

International Atomic Energy Agency. (n.d.). *Diagnostic radiology physics: A handbook for teachers and students.* https://www.iaea.org/resources/rpop/resources/training-material

Kraft, G. (2009). Charged particle therapy: The physics of interaction. *The Cancer Journal.* https://europepmc.org/article/MED/19672144

Laird, A. K. (1964). Dynamics of tumour growth. *British Journal of Cancer, 18*(3), 490-502. https://www.nature.com/articles/bjc196455.pdf

Massachusetts General Brigham. (n.d.). *Bragg peak.* https://radoncphysics.massgeneralbrigham.org/media/com_dpattachments/attachments/com_content.article/Techniques-of-Proton-Radiotherapy-10-Bragg-Peak.pdf

Merchant, T. E. (2018). Clinical controversies: Proton therapy for pediatric tumors. *Seminars in Radiation Oncology, 28*(2). https://pubmed.ncbi.nlm.nih.gov/29485090/

National Cancer Institute. (n.d.-a). *Cancer imaging basics.* https://dctd.cancer.gov/research/research-areas/imaging/basics

National Cancer Institute. (n.d.-b). *Definition of MRI.* https://www.cancer.gov/publications/dictionaries/cancer-terms/def/mri

Nobel Prize Outreach. (n.d.-a). *James Chadwick - Facts.* https://www.nobelprize.org/prizes/physics/1935/chadwick/facts/

Nobel Prize Outreach. (n.d.-b). J. J. *Thomson - Biographical.* https://www.nobelprize.org/prizes/physics/1906/thomson/biographical/

Oigman, G., Osorio, D., Ferman, S. E., Stanek, J., Souto, A. A. D., Christiani, M. M. C., Magalhaes, D. M. A., & Finlay, J. L. (2022). Epidemiological characteristics and survival outcomes of children with medulloblastoma treated at the National Cancer Institute (INCA) in Rio de Janeiro, Brazil. *Pediatric Blood & Cancer, 69,* 1-10. https://doi.org/10.1002/pbc.29274

Palumbo, P., Evangelista, G., Caulo, M., & Splendiani, A. (2023). Magnetic resonance imaging of primary adult brain tumors: State of the art and future perspectives. *Biomedicines, 11*(4), Article 1111. https://pubmed.ncbi.nlm.nih.gov/37238297/

Particle Data Group. (2019). *Passage of particles through matter.* https://pdg.lbl.gov/2019/reviews/rpp2018-rev-passage-particles-matter.pdf

Radiology Key. (n.d.). *X-ray interactions with matter.* https://radiologykey.com/x-ray-interactions-with-matter/

Rojas, D. M. P., Perea Vásquez, L. E., Rojas Torres, I.

L., Perea Molinares, C. M., & Seni Hernández, C. D. (2024). Medulloblastoma in children: A case report and literature review. *Journal of Radiology Case Reports, 18*(8), 40-50. https://www.radiologycases.com/index.php/radiologycases/article/download/5362/2389/24791

Santos, M. O., Lima, F. C. S., Martins, L. F. L., Oliveira, J. F. P., Almeida, L. M., & Cancela, M. C. (2023). Estimated cancer incidence in Brazil, 2023-2025. *Revista Brasileira de Cancerologia, 69*(1). https://rbc.inca.gov.br/index.php/revista/article/view/3700

St. Jude Children's Research Hospital. (n.d.). *Proton beam radiation for pediatric cancer patients.* https://together.stjude.org/en-us/treatment-tests-procedures/treatments/radiation-therapy/proton-beam-radiation.html

Wilson, R. R. (1946). Radiological use of fast protons. *Radiology, 47*(5), 487-491. https://pubs.rsna.org/doi/pdf/10.1148/47.5.487